

Microbial chemolithotrophy mediates oxidative weathering of granitic bedrock

Stephanie A. Napieralski^{a,1}, Heather L. Buss^b, Susan L. Brantley^{c,d}, Seungyeol Lee^a, Huifang Xu^a, and Eric E. Roden^{a,1}

^aDepartment of Geoscience, NASA Astrobiology Institute, University of Wisconsin–Madison, Madison, WI 53706; ^bSchool of Earth Sciences, University of Bristol, BS8 1RJ Bristol, United Kingdom; ^cEarth and Environmental Systems Institute, Pennsylvania State University, University Park, PA 16802; and ^dDepartment of Geosciences, Pennsylvania State University, University Park, PA 16802

Edited by Donald E. Canfield, Institute of Biology and Nordic Center for Earth Evolution, University of Southern Denmark, Odense M., Denmark, and approved November 21, 2019 (received for review June 11, 2019)

The flux of solutes from the chemical weathering of the continental crust supplies a steady supply of essential nutrients necessary for the maintenance of Earth's biosphere. Promotion of weathering by microorganisms is a well-documented phenomenon and is most often attributed to heterotrophic microbial metabolism for the purposes of nutrient acquisition. Here, we demonstrate the role of chemolithotrophic ferrous iron [Fe(II)]-oxidizing bacteria in biogeochemical weathering of subsurface Fe(II)-silicate minerals at the Luquillo Critical Zone Observatory in Puerto Rico. Under chemolithotrophic growth conditions, mineral-derived Fe(II) in the Rio Blanco Quartz Diorite served as the primary energy source for microbial growth. An enrichment in homologs to gene clusters involved in extracellular electron transfer was associated with dramatically accelerated rates of mineral oxidation and adenosine triphosphate generation relative to sterile diorite suspensions. Transmission electron microscopy and energy-dispersive spectroscopy revealed the accumulation of nanoparticulate Fe-oxhydroxides on mineral surfaces only under biotic conditions. Microbially oxidized quartz diorite showed greater susceptibility to proton-promoted dissolution, which has important implications for weathering reactions in situ. Collectively, our results suggest that chemolithotrophic Fe(II)-oxidizing bacteria are likely contributors in the transformation of rock to regolith.

chemolithotrophy | weathering | critical zone

The role of microorganisms in the weathering of minerals has long been recognized (1). More recent interest in the role of Fe(II)-oxidizing bacteria (FeOB) has been driven by the recognition that Fe(II)-bearing mineral phases, such as Fe(II)-silicates and pyrite, represent a potential wealth of energy to fuel chemolithotrophic metabolisms, both terrestrially (2) and on other rocky planetary bodies such as Mars (3). Thus far, the best attempts to characterize the activity of FeOB and their relationship to Fe(II)-silicate weathering come from studies on the subaqueous alteration of the basaltic oceanic crust, where it has been demonstrated that FeOB colonize highly reactive basaltic glasses and form thick microbial mats near hydrothermal vent features (4–6). However, controversy remains as to the ability of these marine microorganisms to directly utilize solid-phase Fe(II) to fuel their metabolisms (7, 8), and it has been suggested that dissolved Fe(II) released is the major energy source for biomass formation in the vicinity of hydrothermal vents (9).

Compared to the extensive studies targeting oceanic systems, investigations into the role of FeOB in continental weathering are more limited. The potential role of FeOB in Fe-silicate weathering has been postulated, the supposition being that redox-driven crystallographic changes should be sufficient to lead to mineral dissolution (10). Although it has been established that structural Fe(II) in biotite is capable of supporting FeOB growth in vitro (11), efforts to more fully characterize the role of bacteria in terrestrial weathering processes (10, 12, 13) and to link FeOB activity to weathering of volcanic rocks (14) have yielded no definitive evidence for the involvement of FeOB in situ. Nevertheless, multiple lines of circumstantial evidence have been presented for the potential involvement of FeOB in the weathering of the

Rio Blanco Quartz Diorite underlying the Rio Icacos watershed of the Luquillo Critical Zone Observatory, Luquillo, Puerto Rico (15–17). The Rio Blanco Quartz Diorite is primarily composed of plagioclase feldspar and quartz with lesser amounts of the Fe(II)-bearing silicate phases biotite (~10 wt%) and hornblende (~7 wt%). It is estimated to have one of the highest weathering fluxes known for a granitic material (18). The regolith developed from the Rio Blanco Quartz Diorite consists of a 1-m-thick soil overlying an oxidized saprolite zone comprising primarily quartz, altered biotite, secondary kaolinite, and goethite, with a variable depth of 2 m to perhaps 30 m (18, 19). The interface of partially altered, fractured rocky material between individual unaltered bedrock corestones and overlying saprolite is termed the “rindlet zone” (20). Here, diffusion of oxygen into the crystalline rock is thought to cause oxidation of biotite, producing strain that ultimately causes the bedrock to fracture and weather spheroidally, exhibiting a concentric, onion-skin-like profile commonly observed during weathering of some granites (21) (Fig. 1, *Inset*). Further oxidative weathering of biotite occurs within the rindlet zone, and the complete depletion of hornblende occurs across a narrow, circa (ca.) 7-cm band of rindlets before the rindlet-saprolite interface

Significance

We utilized the Luquillo Critical Zone Observatory (LCZO) in Puerto Rico to test the hypothesis that mineral-derived Fe(II) within the granitic bedrock at LCZO is capable of supporting microbial Fe(II)-based chemolithotrophy and that the resultant redox-driven mineralogical transformations contribute to bedrock weathering. While this hypothesis had been postulated based on theoretical calculations of Fe(II) loss and potential chemolithotrophic Fe(II)-oxidizing bacterial growth across the bedrock-saprolite interface, to date it has not been verified experimentally. Our study definitively demonstrates the ability of chemolithotrophic Fe(II)-oxidizing bacteria to accelerate oxidative transformation of Fe(II)-silicate minerals. In addition, our work presents insight into complex microbial community interactions, which must be considered when assessing the role of microorganisms in bedrock weathering.

Author contributions: S.A.N., H.L.B., S.L.B., and E.E.R. designed research; S.A.N., H.L.B., and S.L. performed research; S.A.N., S.L., and H.X. analyzed data; and S.A.N. and E.E.R. wrote the paper.

The authors declare no competing interest.

This article is a PNAS Direct Submission.

Published under the PNAS license.

Data deposition: Sequencing data generated in this experiment have been deposited in the Sequence Read Archive of the GenBank database, <https://www.ncbi.nlm.nih.gov/sra> (accession nos. [SRR8611926](https://www.ncbi.nlm.nih.gov/sra) [diorite-oxidizing enrichment culture] and [SRR8611927](https://www.ncbi.nlm.nih.gov/sra) [in situ sample]).

¹To whom correspondence may be addressed. Email: snapierski@wisc.edu or eroden@geology.wisc.edu.

This article contains supporting information online at <https://www.pnas.org/lookup/suppl/doi:10.1073/pnas.1909970117/-DCSupplemental>.

First published December 16, 2019.

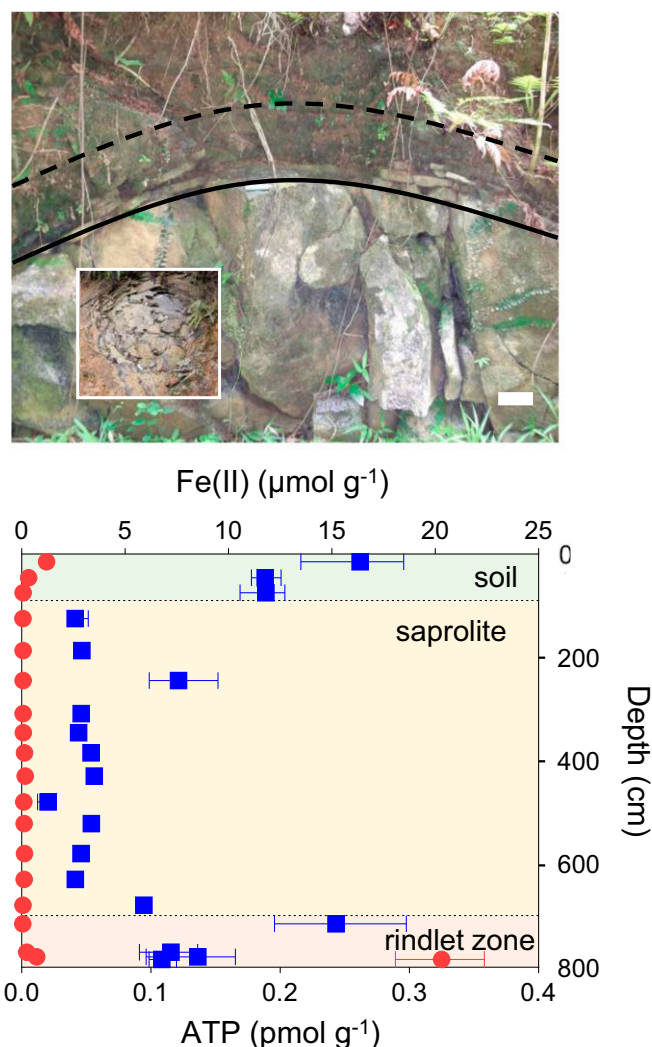


Fig. 1. (Upper) Roadcut exposure of the Rio Blanco Quartz Diorite, used for illustrative purposes to conceptualize the subsurface weathering system at Guaba Ridge within the Rio Icacos watershed of the Luquillo Critical Zone Observatory in Puerto Rico. The rindlet zone, approximately delineated between the solid line (bedrock–rindlet interface) and the dashed line (rindlet–saprolite interface), overlies the corestones of bedrock and is the zone of active weathering targeted in this study. (Scale bar, 10 cm.) Upper, Inset shows a plan view of the rindlet zone exposed elsewhere. (Lower) Total 0.5 M HCl extractable Fe(II) (red circles) and ATP content (blue squares) of the actual subsurface regolith obtained by hand auger atop Guaba Ridge (core A), including soil, saprolite, and the outer rindlet zone, which was partially penetrated with auger refusal occurring prior to reaching the bedrock–rindlet interface (note that the subsurface rindlet zone is substantially thicker than that revealed by the roadcut). Data points and error bars denote the mean and range of triplicate measurements.

(22). Within this zone, an increase in cell density has been reported, consistent with theoretical calculations suggesting that the gradient of Fe(II) generated by weathering across this zone is capable of supporting a robust community of lithotrophic FeOB at depth (15). Accordingly, we observed an increase in microbial biomass, as determined by adenosine triphosphate (ATP) content of the regolith (Fig. 1) relative to the overlying saprolite, indicating the presence of an actively metabolizing microbial community coincident with a sharp gradient in solid-phase Fe(II) at the rindlet–saprolite interface. Within this biogeochemical framework, we sought to test the hypothesis (15) that mineral-derived Fe(II) is capable of supporting chemolithotrophic cellular

growth coupled to Fe(II) oxidation. In addition, electron-microscopic analysis and simulated weathering experiments explored how microbial redox-driven mineralogical transformations may contribute to the documented (15, 18, 20–22) weathering systematics of the Rio Blanco Quartz Diorite.

Results and Discussion

Chemolithotrophic Fe(II)-Oxidizing Enrichment Cultures. Ground (<45 μm) Rio Blanco Quartz Diorite was incubated over a period of ca. 2.4 y (864 d) under imposed chemolithotrophic conditions with natural inocula from 3 separate rindlet–saprolite interface samples (cores A, B, and C). Significant oxidation was observed in the presence of a live inocula compared to sterile abiotic controls. The ratio of Fe(II) to Fe(total) [Fe(tot)] in dilute HCl extracts of solid-phase material declined over time from 76.3 to 43.1% (Fig. 2A) in the most extreme example of microbial oxidation. This change in the dilute HCl-extractable Fe pool corresponded to the oxidation of ca. 0.6% of the total Fe(II) content of the quartz diorite. Given that no significant oxidation occurred under abiotic conditions, our results demonstrate that microbial acceleration of Fe(II)–silicate oxidation was essentially infinite on the time scale of this experiment. ATP abundance, indicating the generation of metabolic energy, was up to an order

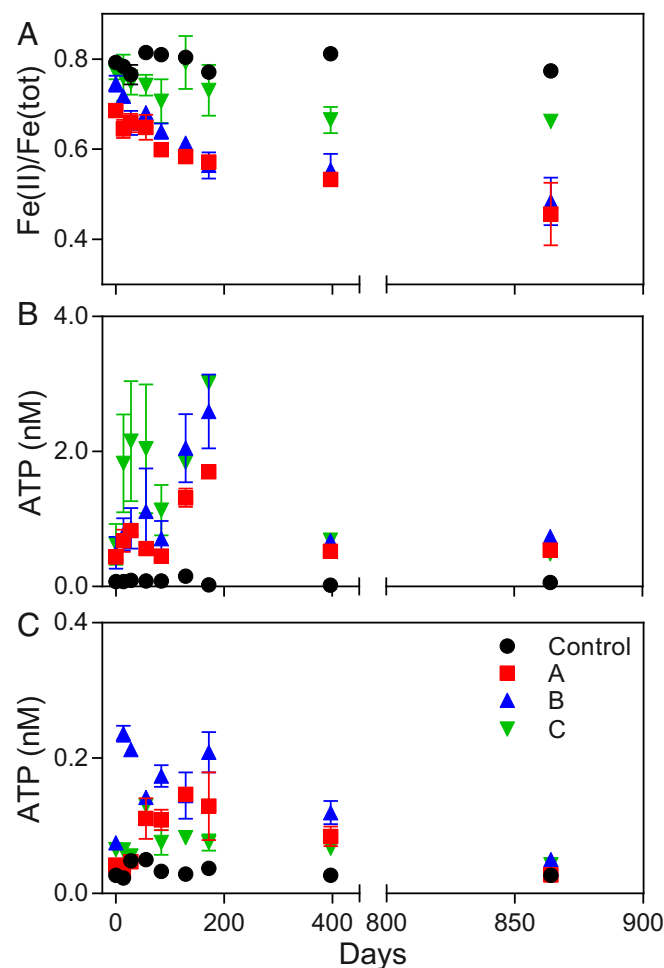


Fig. 2. (A) Molar ratio of Fe(II) to total Fe concentration [Fe(II)/Fe(tot)] in dilute HCl extracts of solid-phase material in quartz diorite enrichment cultures containing 3 separate inocula from the rindlet–saprolite interface (A, B, and C) compared to abiotic uninoculated controls. (B and C) ATP content of cultures containing quartz diorite (B) or quartz sand (C). Data points and error bars denote the mean and range of duplicate cultures.

of magnitude higher in cultures containing diorite compared to cultures provided with pure [Fe(II)-free] quartz sand (Fig. 2 B and C). Both the quartz sand and the quartz diorite had no detectable (<0.005%) particulate organic carbon (POC) content, suggesting that ATP generation was not primarily linked to the oxidation of trace POC in mineral substrates. ATP has been demonstrated to correlate directly with biomass carbon (23, 24). Thus, using a conversion of 10 $\mu\text{mol ATP g}^{-1}$ biomass C (25) and assuming that the pool of dilute HCl-extractable Fe(II) represents Fe(II) available for microbial oxidation (11), microbial growth yields in $\mu\text{mol biomass C } \mu\text{mol}^{-1}$ Fe(II) oxidized were estimated. Biomass yields over the first 172 d (to peak ATP production) from individual reactors inoculated with material from cores A and B were between 0.013 and 0.020 μmol of biomass C μmol^{-1} Fe(II) oxidized (calculations in *SI Appendix, Table S1*), consistent with reported growth yields for neutrophilic chemolithotrophic FeOB in opposing gradient medium (26). Growth yields from reactors inoculated with material from core C were more variable between replicates and higher than would be predicted for Fe(II) oxidation alone. As the extent of oxidation in C reactors was lower than that observed for A and B reactors with comparable ATP production, this observation is best explained by input from alternative metabolisms in core C reactors. However, taken together, these results suggest that the oxidation of mineral-derived Fe(II) in the quartz diorite was the primary source of metabolic energy generation and resultant microbial growth in the majority of reactors. After initial growth, spurred by the availability of fresh mineral surfaces, ATP generation declined across all reactors, while Fe(II) continued to be oxidized, suggesting the establishment of a maintenance condition, whereby individual cells are still metabolizing without actively increasing in biomass.

Shotgun metagenomic analysis revealed that the microbial community in the quartz diorite-oxidizing enrichment culture was dramatically simplified compared to the in situ rindlet-saprolite sample (*SI Appendix, Fig. S1*). The enrichment culture metagenome was dominated by organisms belonging to the Betaproteobacteria, including the genera *Cupriavidus* and *Burkholderia* and the order Neisseriales (*SI Appendix, Fig. S2*). Such organisms have been shown by 16S ribosomal RNA gene-amplicon sequencing surveys to be abundant in weathering systems (10, 27), and the ability of *Cupriavidus necator* to grow by oxidation of Fe-phylosilicate minerals has been demonstrated (28). Taxonomically, the *Neisseriales* species (sp.) in enrichments appears to be closely related to the lithotrophic, Fe(II)-oxidizing, nitrate-reducing organism *Pseudogulbenkiania* sp. strain 2002, which is capable of nitrate-dependent growth on solid-phase Fe(II) (29). In addition to these dominant organisms having taxonomic affinity to described FeOB, 7 metagenome-assembled genomes (MAGs) obtained from the coassembled metagenomes contained homologs to the known Fe(II)-oxidation pathway of the acidophilic FeOB *Acidithiobacillus ferrooxidans* (Fig. 3). In *A. ferrooxidans*, the outer membrane-bound c-type cytochrome Cyc2 is the iron oxidase (30, 31). As is the case with the oxidation of soluble Fe(II) by *A. ferrooxidans*, the oxidation of mineral-bound Fe(II) would necessarily be performed extracellularly (11) with subsequent transport of electrons to the intracellular components of the electron transport chain via a periplasmic electron carrier. This process, termed extracellular electron transfer (EET), was originally recognized in dissimilatory Fe(III)-reducing organisms (32), but has subsequently been shown to be utilized by FeOB (33, 34). Homologs to the Cyc2-type EET system have been found to be present in a broad range of FeOB genomes, including those of aerobic neutrophilic FeOB (33, 35), and recently validated via metaomics (36). Organisms of the genera *Ralstonia* and *Rhodospseudomonas* which are known to harbor FeOB (37, 38) were among the top 10 genera in the enrichment culture based on read classification (*SI Appendix, Fig. S2*); however, no MAGs containing

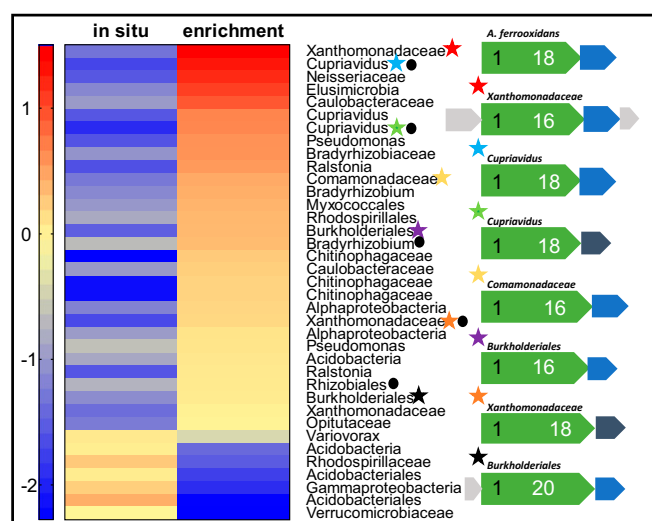


Fig. 3. Heat-map comparison of high-quality MAG abundance (log genomes per million reads) and taxonomy between the in situ bedrock-saprolite interface sample (785-cm depth) and quartz diorite-oxidizing enrichment culture from the same inocula. Stars indicate the presence of homologs to the model Cyc2 iron-oxidation system of *A. ferrooxidans*. Corresponding gene maps (indicated by star color) are shown for each Cyc2 homolog, compared to the model (top). Extracellular or outer-membrane putative Cyc2 proteins (green) are scaled to the size of the protein, with the number of N-terminal heme binding motifs indicated in black and C-terminal transmembrane domains in white. Periplasmic electron carriers including monoheme c-type cytochromes (blue) or high potential iron-sulfur proteins (dark gray) and hypothetical proteins (light gray) are also indicated. Presence of RuBisCo is indicated by a circle.

EET pathways of these genera were obtained. Additionally, while ectomycorrhizal fungi have been noted to oxidatively weather structural Fe(II) in biotite (39), fungal-associated sequences were not detected in the raw reads for either metagenome or the coassembled metagenome, likely due to the extremely low organic carbon content at the bedrock-saprolite interface (15) and the chemolithotrophic culturing conditions in our experiments.

Many chemolithotrophic organisms are capable of growing autotrophically, most commonly by the use of the ubiquitous enzyme ribulose-1,5-bisphosphate carboxylase (RuBisCo), which serves as the entry point for inorganic carbon into the Calvin cycle. Of the MAGs that contained putative EET pathways, 3 also contained the complete RuBisCo system, including 2 *Cupriavidus* MAGs (Fig. 3), which supports the idea that these organisms can grow chemolithoautotrophically. Notably, there are multiple MAGs with putative EET pathways that do not contain RuBisCo, including a *Xanthomonadaceae*, most closely related to the soil bacterium *Dyella japonica*. Though not described as Fe(II) oxidizers, a homolog to Cyc2 gene was also found in the non-autotrophic *D. japonica* A8 (40). While chemolithoheterotrophy is a less common metabolic strategy than chemolithoautotrophy and remains to be validated in *Dyella* sp., the potential for Fe(II) chemolithoheterotrophy cannot be discounted. Mapping of the metagenomic reads from individual samples back to each MAG from the coassembled metagenome reveals that the putative chemolithotrophs became enriched in the diorite-oxidizing cultures relative to the in situ sample (Fig. 3).

Mineralogical and Geochemical Effects of FeOB Activity. Potential mineralogical changes associated with FeOB activity in the enrichment cultures were assessed via field emission scanning electron microscopy (FE-SEM) and transmission electron microscopy (TEM) with selected area electron diffraction (SAED).

Inspection of whole biotite grains revealed a roughening of grain edges after incubation with live inocula that was not observed after abiotic incubation over the same time period. Significant alteration of the basal plane of biotite was observed (Fig. 4). Etch pits, noted to be formed by siderophore-promoted dissolution (41), were not observed on hornblende surfaces. However, microbially oxidized hornblende surfaces displayed other subtle differences in morphology suggestive of surface alteration (Fig. 5). Upon further inspection via bright-field TEM, nano-sized particles were found along the basal plane of microbially oxidized biotite and the edges of the surface steps of hornblende (Fig. 6). Initial time-0 samples from inoculated cultures displayed clean biotite and hornblende crystal surfaces (Fig. 6). The lack of these features in the inoculated samples at time 0, as well as their absence after 864 d of abiotic incubation (*SI Appendix, Figs. S3 and S4*), implies that the nanoparticles were generated over the course of the experiment by microbial oxidation and not acquired when the weathered inocula were added to the fresh diorite. TEM-energy-dispersive X-ray spectroscopy (EDS) spectra demonstrated that the nanoparticles are Fe-oxyhydroxides, as indicated by Fe enrichment on the microbially oxidized surfaces compared to clean surfaces (Fig. 6). The iron oxyhydroxides were around 3 to 5 nm, similar in size to common examples of ferrihydrite (42), suggesting that the precipitation of ferrihydrite on the surface of Fe-bearing minerals was triggered by microbial oxidation.

In addition to the accumulation of nano-sized Fe-oxyhydroxides, small but significant differences were observed in the total amount of silicon (Si) released from the diorite in the biotic vs. abiotic reactors. Although the aqueous concentration of Si was indistinguishable between these treatments (Fig. 7), the biotic reactors showed a 13 to 40% increase (relative to abiotic controls and time-0 samples) in the amount of Si that was released via extraction with NaOH to raise the pH and desorb any Si that

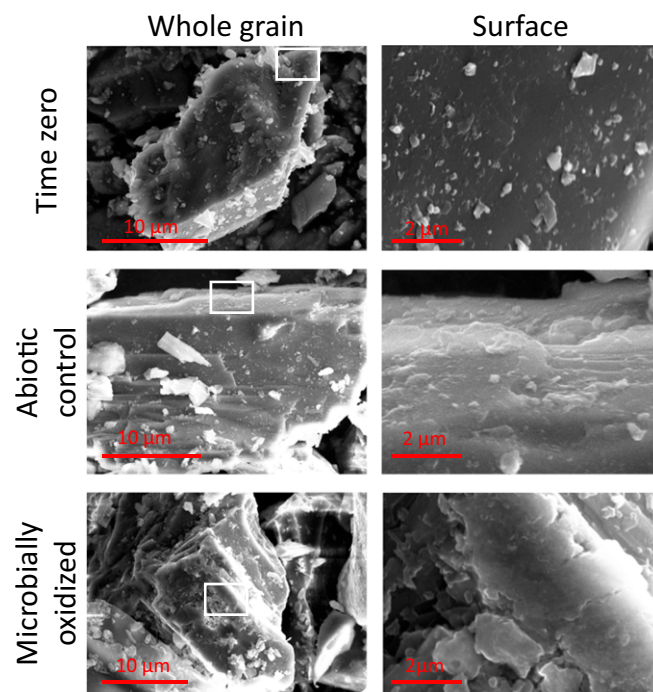


Fig. 5. FE-SEM images of hornblende at the whole-grain scale (Left) and surface scale (Right). Note the differences in scale on whole-grain images, as individual grain sizes are variable. For consistency, surface images are at the same scale. The approximate area of the hornblende surfaces is outlined in white on the grain-scale image.

may have been associated with Fe-oxyhydroxides (43). As a result, there was a significant (2-tailed $P = 0.0398$) increase in total Si release accompanying the microbial oxidation.

No significant differences in the aqueous concentrations of major cations (Mg, Ca, K, and Na) were observed between microbially oxidized and abiotic or time-0 controls. This observation is in contrast to numerous studies on microbially mediated weathering which have demonstrated enhanced release of major rock-forming cations during incubation under heterotrophic conditions (44–46). While initially surprising, it is important to consider the mechanistic differences in mineral dissolution under chemolithotrophic vs. heterotrophic conditions. It is well known that heterotrophically driven dissolution involves acidolysis and chelation by organic ligands (10). In the absence of respiratory CO_2 generation or low-molecular-weight organic acids produced as either a by-product of heterotrophic metabolism or extracellular secretion for nutrient acquisition and/or biofilm formation, one would not expect acidolysis or chelation to be the dominant weathering mechanism under the chemolithotrophic, circum-neutral pH conditions of our experiments. It has been noted that microscale pH gradients within microbial biofilms on colonized silicate minerals can be lowered as much as 1.1 pH units compared to bulk pH (47). Epifluorescence microscopy demonstrated preferential cellular association with solid mineral phases (*SI Appendix, Fig. S5*), where cells appeared as sparse, singular entities along mineral edges (*SI Appendix, Fig. S6*). Similarly diffuse, monolayered biofilms have been observed under the carbon-limited colonization of basaltic glasses (8). As such, localized biofilm acidolysis is also likely to be insignificant (46). Low-molecular-weight organic acids generated from the partial oxidation of glucose, in addition to siderophores, also act as effective chelators. Chelation has been noted to be an important driver of silicate dissolution at near-neutral pH (48), with several studies noting the effect of siderophores in enhancing solubilization of

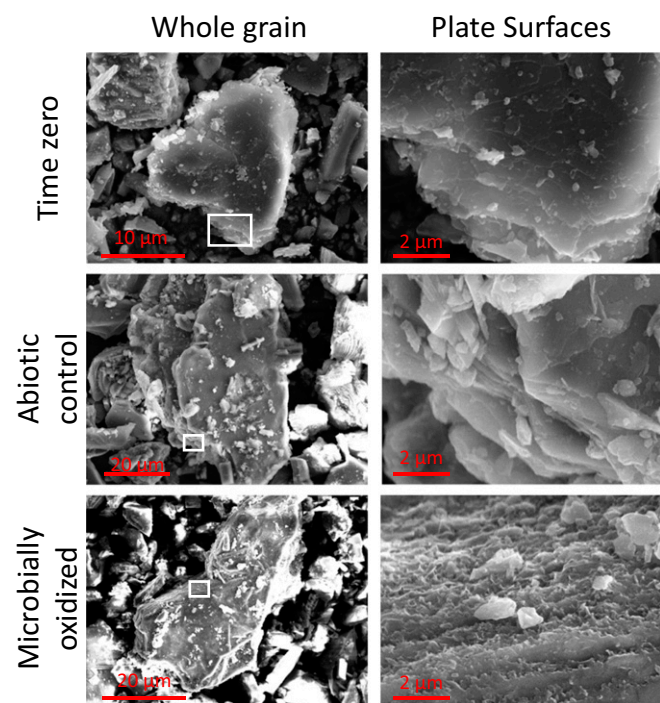


Fig. 4. FE-SEM images of biotite at the whole-grain scale (Left) and basal plane (Right). Note the differences in scale on whole-grain images, as individual grain sizes are variable. For consistency, basal-plane images are at the same scale. The approximate area of the basal plane presented is outlined in white on the grain-scale images. Note the ragged appearance of the basal plane observed after microbial incubation.

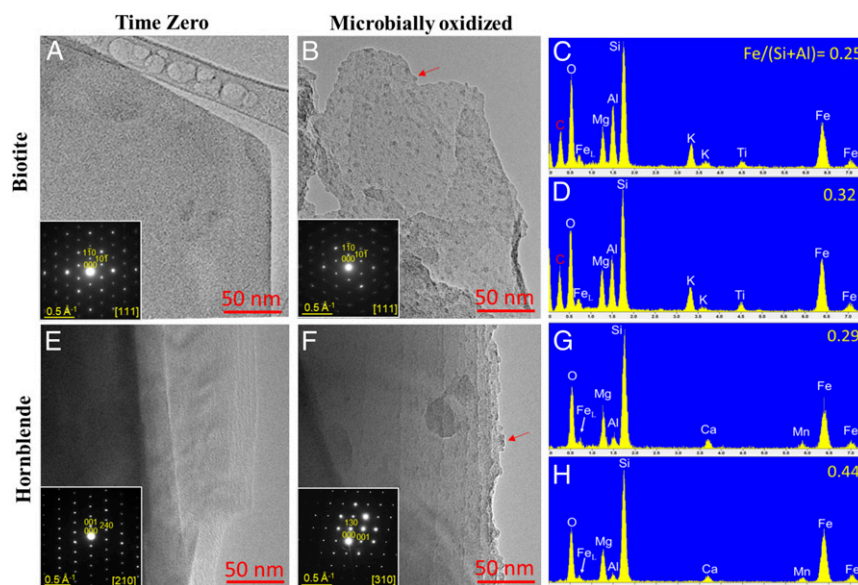


Fig. 6. (A, B, E, and F) Bright-field TEM images and SAED patterns (*Insets*) showing widespread nano-sized Fe-oxhydroxide particles (examples indicated by arrows) along the basal plane of microbially oxidized biotite (B) and surface steps of hornblende (F), which were absent in unoxidized time 0 samples (A and E). (C, D, G, and H) The size (ca. 3 to 5 nm) of the Fe-oxhydroxides is consistent with ferrihydrite. X-ray TEM-EDS spectra confirm the enrichment of Fe [as indicated by the Fe/(Si+Al) atomic ratio] on both microbially oxidized biotite (D) and hornblende (H) compared to initial time-0 surfaces (C and G).

cations during silicate mineral dissolution (41, 49, 50). Given that siderophores are produced specifically for Fe(III) acquisition as a micronutrient under Fe(III) stress (51), their activity would not be expected to produce the oxidative weathering trend observed in this study. While it is not possible to totally rule out the activity of siderophores in this experiment, the data are not consistent with chelation as a primary driver of oxidative weathering under our experimental conditions. Rather, our data collectively point to direct enzymatic oxidation of mineral-derived Fe(II) by chemolithotrophic iron oxidizers for metabolic energy generation. This model is consistent with reported models of in situ weathering, where biological cycling of Fe in the deep saprolite has been inferred based on isotopic measurements (52) and both heterotrophic and lithotrophic microorganisms have been detected at the rindlet-saprolite interface (16, 17). Fe and Mn precipitates previously observed in the outer rindlets, interpreted to result from downward infiltration Fe- and Mn-rich fluids (53), could instead be the result of mobilization and reprecipitation of iron by local oxidative weathering by FeOB in the outer rindlet zone, where these organisms are expected to be of importance.

Enhanced Weatherability of Microbially Oxidized Diorite. Under the imposed chemolithotrophic conditions and considering the proposed mechanism of a direct enzymatic attack on mineral-derived Fe(II) at circumneutral pH, it follows that complete stoichiometric dissolution of the Fe(II)-silicate mineral would not immediately occur and would not be evident over the relatively short time period of this experiment. Rather, Fe(III) may be partially expelled from the crystal lattices to compensate for the charge imbalance created by oxidation, which would likely result in decreased structural integrity of the mineral, as studies have shown (11). This mechanism is consistent with the accumulation of nano-sized Fe-oxhydroxides on biotite and hornblende surfaces (Fig. 6). It is well noted that crystallographic defects and dislocations are sites of preferential weathering in minerals such as hornblende (54). Thus, it may be envisioned that microbially oxidized minerals would be more susceptible to other modes of chemical weathering, including proton-promoted dissolution owing to the inherent disruption of the mineral structure. To address this hypothesis, a portion of the microbially

oxidized quartz diorite was extracted for 24 h in 10 mM HNO₃, followed by analysis of major cation concentrations in the dilute acid extract, measured by inductively coupled plasma optical emission

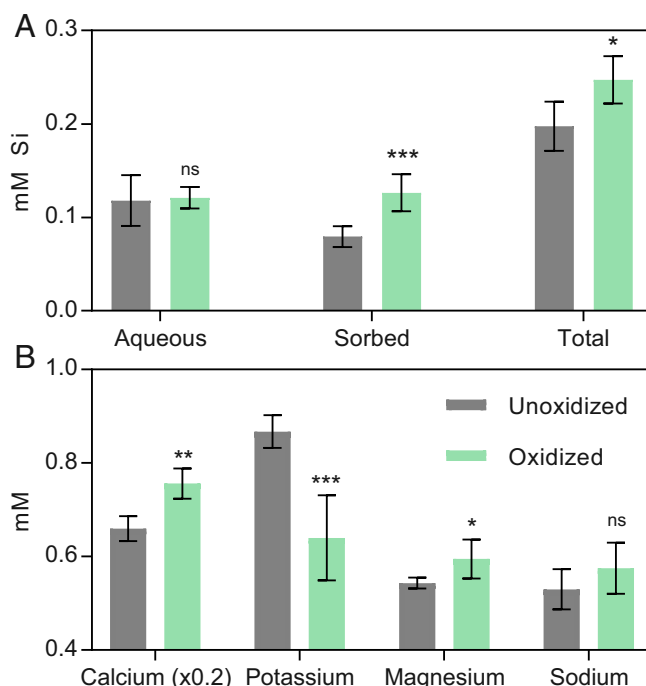


Fig. 7. (A) Concentrations of aqueous, sorbed, and total Si released from unoxidized (combined time-0 and abiotic controls) and microbially oxidized quartz diorite (A, B, and C) after 864 d of incubation. (B) Concentrations of HNO₃-extractable cations released from unoxidized microbially oxidized samples (A, B, and C). For both graphs, $n = 6$ for microbially oxidized samples (duplicate cultures from 3 inocula after 864 d), and $n = 10$ for unoxidized (duplicate cultures from time 0 for 3 inocula and abiotic control and the abiotic control after 864-d incubation). Two-tailed P values for unpaired t test between unoxidized and microbially oxidized are indicated. * $P < 0.05$; ** $P < 0.01$; *** $P < 0.001$. ns, not significant.

spectroscopy (ICP-OES). HNO_3 -extractable Ca and Mg were significantly (2-tailed $P = 0.0120$ and 0.0470 , respectively) elevated in microbially oxidized quartz diorites relative to the unoxidized controls (Fig. 7). Major sources of these 2 cations in the Rio Blanco Quartz diorite included hornblende, biotite, and plagioclase (Na,Ca-feldspar). In the case of biotite, which would be the dominant source of K in addition to a source of Mg, HNO_3 -extractable K was significantly ($P = 0.0010$) lower in biotic reactors than in abiotic controls. It has been shown that the extractability of K from biotite is related to the oxidation state of the octahedral iron, with higher K retention correlating to increased oxidation of structural Fe(II) (55–57). It has also been observed that oxidized biotites in natural weathering systems can retain significant portions of their K (58). Although K does become depleted (relative to the bedrock) within and above the rindlet-saprolite interface (22), this depletion is attributed to continual removal by fluid flow within microcracks in the rindlet interiors that form during quartz diorite weathering. Because such fluid flow was absent in our incubation experiments, the repression of K release upon acid extraction observed here is best explained by enhanced retention linked to a decrease in structural Fe(II) in biotite within the closed reaction system. While it is likely that some dissolution of plagioclase contributed to the observed aqueous chemistry, the lack of Fe in its mineral structure makes it generally unresponsive to the activity of FeOB. As such, any dissolution of the relatively sodic plagioclase (compared to other rock constituents) upon acid treatment would be expected to be comparable between oxidized and unoxidized diorites. The lack of significant difference (2-tailed $P = 0.1429$) in acid-extractable Na concentrations between unoxidized control and microbially oxidized diorites is consistent with this idea and suggests that the difference in acid-extractable Ca, Mg, and K between control and oxidized diorites was linked to reduced structural integrity of ferromagnesian minerals as a result of prior FeOB activity.

Conclusions

This study demonstrates that chemolithotrophic FeOB inhabiting the rindlet-saprolite interface of the Rio Blanco Quartz Diorite are capable of growing on mineral-derived Fe(II) as their primary source of metabolic energy, utilizing genomically encoded EET pathways. The enrichment of these organisms under imposed chemolithotrophic conditions points to their potential to be involved in the subsurface weathering of the Rio Blanco Quartz Diorite. In contrast to the ground quartz diorite used in this experiment, the slow diffusion of oxygen into low-porosity fresh bedrock is posited to be necessary for the initial fracturing that forms the rindlet zone (53) and therefore likely modulates weathering over geologic time scales. However, once porosity is sufficient to allow advective transport of fluids and microbial colonization along cracks and fractures, in light of the results of this study, it seems likely that that FeOB play an important role in the overall weathering regime of the Rio Blanco Quartz Diorite, particularly within the saprolite-adjacent part of the rindlet zone, where rapid depletion of mineral-bound Fe(II) is observed. The fact that microbially oxidized quartz diorites were more susceptible to proton-promoted dissolution also has important implications for the effectiveness of acidolysis and/or chelation weathering processes associated with heterotrophic microbial metabolism. While the focus of the study was exclusive to the role of FeOB in Fe(II) silicate weathering, and care must be taken when extrapolating laboratory studies to events in natural systems, our findings point clearly to the need for further investigation into the interplay between chemolithotrophically and heterotrophically driven silicate mineral weathering.

Methods

Field Sampling. In June 2016, 3 cores (A, B, and C) were taken from saprolite atop Guaba Ridge at the Luquillo Critical Zone Observatory by hand auger to the depth of refusal (i.e., into the outer rindlet zone), which varied from 248 cm (core B) to 785 cm (core A), with core C being of intermediate depth (627 cm), reflecting the topology of the bedrock beneath Guaba Ridge. All cores were taken within close proximity to an established lysimeter field (18, 59), and care was taken to avoid repeat sampling of sites previously cored. Samples were collected aseptically at ~40- to 50-cm intervals for core A, as described (15). Cores B and C were sampled intermittently. Material collected was shipped overnight to the University of Wisconsin–Madison (UW–Madison) on blue ice packs, and portions were either refrigerated at 4 °C for live culturing or frozen at –80 °C upon arrival for DNA extraction. The 0.5-g aliquots of each sample were placed in 20 mM EDTA and frozen at –80 °C for ATP analysis.

Chemolithotrophic Enrichment Culturing. Solid-phase mineral-oxidizing enrichment cultures were established by using whole-rock Rio Blanco Quartz Diorite obtained from a road-cut exposure. Mineral stoichiometries and abundances were determined by White et al. (18); bulk elemental abundances (aqua regia digestion and ICP-OES analysis; ALS Geochemistry) are provided in *SI Appendix, Table S2*. Following collection, external weathered surfaces were removed by using a rock saw. Large pieces of quartz diorite were fragmented by using a jaw crusher to obtain suitable-sized fractions for further pulverization using a shatter box. Shattered quartz diorite was sieved to <45 μm . Luquillo artificial groundwater (L-AGW) was prepared to a final millimolar solution concentration of 0.06 $\text{MgCl}_2 \cdot 6\text{H}_2\text{O}$, 0.04 KH_2PO_4 , 0.05 NaNO_3 , 0.1 NaHCO_3 , 0.03 $\text{Ca}(\text{NO}_3)_2 \cdot 4\text{H}_2\text{O}$, and 0.01 Na_2SO_4 . All glassware was combusted overnight at 550 °C to minimize carbon contamination. In an anaerobic chamber, 5.0 g of pulverized quartz diorite or pure quartz sand (Acros Chemicals; 140 to 381 μm) was placed in a 120-mL bottle, and 50 mL of anoxic L-AGW was added. Bottles were crimp sealed with a rubber stopper and autoclaved. After sterilization, the headspace was flushed with sterile air to render the cultures aerobic. Duplicate reactors of each mineral treatment (quartz diorite or quartz) were inoculated with ca. 1.0 g of material from 1 of the 3 (A, B, or C) samples obtained from the rindlet-saprolite interface, stoppered, and incubated in the dark. Duplicate abiotic controls for each treatment were aerated and left uninoculated. We added 5.0% (volume) CO_2 to the headspace of each bottle as a carbon source for autotrophic growth. The pH of reactors after equilibration with CO_2 and mineral phases was circumneutral (6.7 to 7) in all reactors. Samples were taken immediately following inoculation and after 14; 28; 56; 84; 129; 172; 397; and 864 d.

Analytical Techniques.

ATP. A total of 0.5 mL of mineral suspension was placed into cold 20 mM EDTA and vortexed and immediately frozen at stored –80 °C prior to ATP biomass determination. At the time of analysis, samples for ATP were thawed, vortexed once more, and centrifuged. ATP content of the supernatant was determined via luminescence by using BacTiter-Glo (Promega), with calibration to a standard curve prepared in 20 mM EDTA.

Solid-phase Fe(II). The ratio of Fe(II) to total Fe released by 0.5 M HCl extraction was determined on in situ core samples and the solids from 1.0 mL of enrichment culture subsamples. The solids were extracted for 24 h in 5 mL of 0.5 M HCl on an orbital shaker. For natural samples, 0.5 g of regolith was added directly to acid for 24-h extraction. Fe(II) of each extract was determined by the standard Ferrozine assay (60), and the measurement was repeated after the addition of hydroxylamine–HCl for determination of Fe(tot), with Fe(III) determined by difference.

POC. Particulate organic matter of the Rio Blanco Quartz Diorite and Fe(II)-free quartz sand was determined via high-temperature combustion by using a Flash EA 1112 Flash Combustion Analyzer.

Cations. Major cation concentrations (Ca, K, Mg, Na, and Si) in the aqueous phase of the cultures were determined by using ICP-OES using a Varian Vista-MPX ICP-OES. The aqueous phase from duplicate reactors was pooled, filtered through a 0.22- μm filter, and diluted 1:5 in Milli-Q water. Samples were run unacidified to avoid precipitation of Si, with standards prepared for an appropriate calibration curve also in Milli-Q water.

Silica. At the termination of the experiment, any sorption of Si to biogenic Fe-(oxy)hydroxides was assessed by high pH desorption. A total of 1.0 mL of culture was aseptically removed and centrifuged to pellet the solids. The supernatant was removed, and an equal volume of 10 mM NaOH was added to the remaining solids. The slurry was agitated for 24 h, and the supernatant was recovered by centrifugation. Si content was determined spectrophotometrically by using the heteropoly blue assay. Following verification of

consistency between ICP-OES and heteropoly blue Si determination, total Si release at 864 d was calculated as the sum of aqueous Si and sorbed Si.

Epifluorescence microscopy. Subsamples of live inoculated and abiotic control cultures were taken at 196 d for epifluorescence microscopy. Whole culture solution was immediately stained with DAPI (ThermoFisher Scientific), following manufacturer's protocols, and imaged on a Nikon E600 compound phase-contrast epifluorescence microscope.

Proton-Promoted Dissolution Determination. The susceptibility of oxidized and unoxidized quartz diorites to proton-promoted dissolution was assessed as described (61) for mineral acid dissolution to avoid ambiguity regarding the potential dual role of organic acids as chelators. After 864 d, 1.0 mL of culture from each inocula and the abiotic control were pelleted via centrifugation to recover the solid phase. The supernatant was removed, an equal volume of 10 mM HNO₃ was added, and the slurry was agitated for 24 h on an orbital shaker. The aqueous phase was collected via centrifugation and passed through a 0.22-μm filter. Individual samples were diluted 1:5 in HNO₃ for ICP-OES analysis. Cation concentrations (Ca, K, Mg, and Na) were determined by calibration to a standard curve prepared in 10 mM HNO₃. To assess any differences that may have arisen as a consequence of the inclusion of natural weathered material as inocula at time 0, all samples were compared to the initial conditions (time 0) for their respective inocula (A, B, or C), or fresh diorite in the case of the abiotic control.

Mineralogical Analysis. Samples were prepared for FE-SEM by dropping whole, undiluted liquid culture suspensions of time 0, a microbially oxidized sample inoculated with core A material (the same sample for which the metagenome was obtained), and an abiotically incubated control onto carbon tape affixed to a stub mount. Samples were air dried and carbon coated prior to imaging. Images were acquired by using a Cameca SXFiveFE with an accelerating voltage of 15 kV. TEM samples were prepared for the same samples as FE-SEM by dropping suspensions of crushed samples onto lacy-carbon-coated 200-mesh Cu grids. TEM imaging and SAED analysis were carried out by using a Philips CM200-UT microscope operated at 200 kV in the Materials Science Center at UW–Madison. The chemical composition was obtained by using a TEM-EDS system equipped with an Li-drifted Si detector (Oxford Instruments Link ISIS). An electron-beam diameter of ~50 nm was used for collecting X-ray EDS spectra.

DNA Extraction, Sequencing, and Metagenomic Analysis. DNA was extracted from in situ core samples and enrichment culture subsamples via the sodium dodecyl sulfate-based extraction method adapted from Zhou et al. (62). Reagent volumes were appropriately scaled to accommodate 0.5-g extrac-

tions, and 2 volumes of ethanol was used for DNA precipitation at –20 °C. Crude DNA was resuspended in 50 μL of 10 mM Tris (pH 8). Multiple extractions were performed until a sufficient mass of DNA for metagenomic sequencing was reached. Replicate extracts were cleaned and pooled by using Zymo Clean and Concentrator-5 (Zymo Research). Enrichment culture DNA from the 129-d sample was obtained via pelleting 2.0 mL of culture and extraction of solids using the same method as above.

DNA was submitted to the UW–Madison Biotechnology Center for metagenomic library preparation and 2 × 250 paired-end sequencing on the Illumina HiSeq 2500 Rapid platform. Raw reads were quality trimmed to remove low-quality sequences. Taxonomy of individual reads was estimated by using Kraken (63) and the standard Kraken database. Reads from individual metagenomic libraries were concatenated and coassembled by using IDBA-UD (64), utilizing the high-performance computing cluster in the Center for High Throughput Computing at UW–Madison. Assembled contigs were clustered into phylogenetic bins by using MetaBAT (Version 2.12.1) (65). The bin set was evaluated for completion and contamination by using CheckM (66). Consensus taxonomy of individual bins was determined by using single-copy housekeeping genes identified in CheckM and MegaBLAST (67) alignment of individual contigs to the National Center for Biotechnology nucleotide database using metaWRAP (68). Blobology (69) was used to visualize and compare the microbial community compositions. Quantification of the abundance of each bin across samples was performed within the bin-quantification module of metaWRAP. Individual bins were reassembled, producing a final set of MAGs deemed to be of high quality if greater than 70% complete and less than 10% redundant. MAGs were screened for putative extracellular electron transfer pathways as described (35).

Data Analysis. Unpaired *t* tests were used in statistical comparison between unoxidized (time 0 and control) and microbially oxidized (A, B, C) using GraphPad Prism (Version 7.05). Two-tailed *P* values are reported.

Data Availability. Sequencing data generated in this experiment have been deposited in the Sequence Read Archive (SRA) of the GenBank database under the accession numbers SRR8611926 and SRR8611927, the diorite-oxidizing enrichment culture and in situ sample, respectively.

ACKNOWLEDGMENTS. We thank the NSF Luquillo Critical Zone Observatory (LCZO) for access to facilities and assistance with fieldwork. This work was supported by the NASA Astrobiology Institute and a University of Wisconsin Microbiome Initiative award (to E.E.R.). S.L.B. and H.L.B. were supported by the LCZO (NSF Grants EAR-0722476 and EAR-1331841).

1. J. F. Banfield, W. W. Barker, S. A. Welch, A. Taunton, Biological impact on mineral dissolution: Application of the lichen model to understanding mineral weathering in the rhizosphere. *Proc. Natl. Acad. Sci. U.S.A.* **96**, 3404–3411 (1999).
2. W. Bach, K. J. Edwards, Iron and sulfide oxidation within the basaltic ocean crust: Implications for chemolithoautotrophic microbial biomass production. *Geochim. Cosmochim. Acta* **67**, 3871–3887 (2003).
3. B. M. Jakosky, E. L. Shock, The biological potential of Mars, the early Earth, and Europa. *J. Geophys. Res.* **103**, 19359–19364 (1998).
4. K. J. Edwards et al., Ultra-diffuse hydrothermal venting supports Fe-oxidizing bacteria and massive unbranched deposition at 5000 m off Hawaii. *ISME J.* **5**, 1748–1758 (2011).
5. C. M. Santelli et al., Abundance and diversity of microbial life in ocean crust. *Nature* **453**, 653–656 (2008).
6. L. A. Sudek, G. Wanger, A. S. Templeton, H. Staudigel, B. M. Tebo, Submarine basaltic glass colonization by the heterotrophic Fe(II)-oxidizing and siderophore-producing deep-sea bacterium *Pseudomonas stutzeri* V5-10: The potential role of basalt in enhancing growth. *Front. Microbiol.* **8**, 363 (2017).
7. M. Y. Xiong, E. S. Shelobolina, E. E. Roden, Potential for microbial oxidation of ferrous iron in basaltic glass. *Astrobiology* **15**, 331–340 (2015).
8. B. Bailey, A. Templeton, H. Staudigel, B. M. Tebo, Utilization of substrate components during basaltic glass colonization by *Pseudomonas* and *Shewanella* isolates. *Geomicrobiol. J.* **26**, 648–656 (2009).
9. A. S. Templeton et al., A seafloor microbial biome hosted within incipient ferromanganese crusts. *Nat. Geosci.* **2**, 872–876 (2009).
10. S. Uroz, C. Calvaruso, M. P. Turpault, P. Frey-Klett, Mineral weathering by bacteria: Ecology, actors and mechanisms. *Trends Microbiol.* **17**, 378–387 (2009).
11. E. Shelobolina et al., Microbial lithotrophic oxidation of structural Fe(II) in biotite. *Appl. Environ. Microbiol.* **78**, 5746–5752 (2012).
12. S. Uroz et al., Functional assays and metagenomic analyses reveals differences between the microbial communities inhabiting the soil horizons of a Norway spruce plantation. *PLoS One* **8**, e55929 (2013).
13. B. Wild et al., In-situ dissolution rates of silicate minerals and associated bacterial communities in the critical zone (Strengbach catchment, France). *Geochim. Cosmochim. Acta* **249**, 95–120 (2019).
14. C. S. Cockell, Life in the lithosphere, kinetics and the prospects for life elsewhere. *Philos. Trans. A Math. Phys. Eng. Sci.* **369**, 516–537 (2011).
15. H. L. Buss et al., The coupling of biological iron cycling and mineral weathering during saprolite formation, Luquillo Mountains, Puerto Rico. *Geobiology* **3**, 247–260 (2005).
16. S. J. Hall et al., Drivers and patterns of iron redox cycling from surface to bedrock in a deep tropical forest soil: A new conceptual model. *Biogeochemistry* **130**, 177–190 (2016).
17. M. L. Minyard et al., Bacterial associations with weathering minerals at the regolith-bedrock interface, Luquillo experimental forest, Puerto Rico. *Geomicrobiol. J.* **29**, 792–803 (2012).
18. A. F. White et al., Chemical weathering in a tropical watershed, Luquillo Mountains, Puerto Rico: I. Long-term versus short-term weathering fluxes. *Geochim. Cosmochim. Acta* **62**, 209–226 (1998).
19. J. Orlando et al., Architecture of the deep critical zone in the Rio Icacos watershed (Luquillo Critical Zone Observatory, Puerto Rico) inferred from drilling and ground penetrating radar (GPR). *Earth Surf. Process. Landf.* **41**, 1826–1840 (2016).
20. B. F. Turner, R. F. Stallard, S. L. Brantley, Investigation of in situ weathering of quartz diorite bedrock in the Rio Icacos basin, Luquillo Experimental Forest, Puerto Rico. *Chem. Geol.* **202**, 313–341 (2003).
21. R. Fletcher, H. Buss, S. Brantley, A spheroidal weathering model coupling porewater chemistry to soil thicknesses during steady-state denudation. *Earth Planet. Sci. Lett.* **244**, 444–457 (2006).
22. H. L. Buss, P. B. Sak, S. M. Webb, S. L. Brantley, Weathering of the Rio Blanco quartz diorite, Luquillo Mountains, Puerto Rico: Coupling oxidation, dissolution, and fracturing. *Geochim. Cosmochim. Acta* **72**, 4488–4507 (2008).
23. D. L. Balkwill, F. R. Leach, J. T. Wilson, J. F. McNabb, D. C. White, Equivalence of microbial biomass measures based on membrane lipid and cell wall components, adenosine triphosphate, and direct counts in subsurface aquifer sediments. *Microb. Ecol.* **16**, 73–84 (1988).
24. D. S. Jenkinson, S. A. Davidson, D. S. Powlson, Adenosine triphosphate and microbial biomass in soil. *Soil Biol. Biochem.* **11**, 521–527 (1979).
25. M. Contin, A. Todd, P. C. Brookes, The ATP concentration in the soil microbial biomass. *Soil Biol. Biochem.* **33**, 701–704 (2001).

26. D. Sobolev, E. Roden, Characterization of a neutrophilic, chemolithoautotrophic Fe(II)-oxidizing β -proteobacterium from freshwater wetland sediments. *Geomicrobiol. J.* **21**, 1–10 (2004).
27. C. Lepleux, M. P. Turpault, P. Oger, P. Frey-Klett, S. Uroz, Correlation of the abundance of betaproteobacteria on mineral surfaces with mineral weathering in forest soils. *Appl. Environ. Microbiol.* **78**, 7114–7119 (2012).
28. E. Shelobolina et al., Isolation of phyllosilicate-iron redox cycling microorganisms from an illite-smectite rich hydromorphic soil. *Front. Microbiol.* **3**, 134 (2012).
29. K. A. Weber, F. W. Picardal, E. E. Roden, Microbially catalyzed nitrate-dependent oxidation of biogenic solid-phase Fe(II) compounds. *Environ. Sci. Technol.* **35**, 1644–1650 (2001).
30. C. Appia-Ayme, N. Guilian, J. Ratouchniak, V. Bonnefoy, Characterization of an operon encoding two c-type cytochromes, an aa(3)-type cytochrome oxidase, and rusticyanin in *Thiobacillus ferrooxidans* ATCC 33020. *Appl. Environ. Microbiol.* **65**, 4781–4787 (1999).
31. C. Castelle et al., A new iron-oxidizing/O₂-reducing supercomplex spanning both inner and outer membranes, isolated from the extreme acidophile *Acidithiobacillus ferrooxidans*. *J. Biol. Chem.* **283**, 25803–25811 (2008).
32. D. R. Lovley, D. E. Holmes, K. P. Nevin, Dissimilatory Fe(III) and Mn(IV) reduction. *Adv. Microb. Physiol.* **49**, 219–286 (2004).
33. R. A. Barco et al., New insight into microbial iron oxidation as revealed by the proteomic profile of an obligate iron-oxidizing chemolithoautotroph. *Appl. Environ. Microbiol.* **81**, 5927–5937 (2015).
34. J. Liu et al., Identification and characterization of MtoA: A decaheme c-type cytochrome of the neutrophilic Fe(II)-oxidizing bacterium *Sideroxydans lithotrophicus* ES-1. *Front. Microbiol.* **3**, 37 (2012).
35. S. He, R. A. Barco, D. Emerson, E. E. Roden, Comparative genomic analysis of neutrophilic iron(II) oxidizer genomes for candidate genes in extracellular electron transfer. *Front. Microbiol.* **8**, 1584 (2017).
36. S. M. McAllister et al., Validating the Cyc2 neutrophilic Fe oxidation pathway using meta-omics of *Zetaproteobacteria* iron mats at marine hydrothermal vents. *bioRxiv*: 10.1101/722066 (1 August 2019).
37. E. D. Swanner, R. M. Nell, A. S. Templeton, *Ralstonia* species mediate Fe-oxidation in circumneutral, metal-rich subsurface fluids of Henderson mine, CO. *Chem. Geol.* **284**, 339–350 (2011).
38. Y. Jiao, A. Kappler, L. R. Croal, D. K. Newman, Isolation and characterization of a genetically tractable photoautotrophic Fe(II)-oxidizing bacterium, *Rhodospseudomonas palustris* strain TIE-1. *Appl. Environ. Microbiol.* **71**, 4487–4496 (2005).
39. S. Bonneville, A. W. Bray, L. G. Benning, Structural Fe(II) oxidation in biotite by an ectomycorrhizal fungi drives mechanical forcing. *Environ. Sci. Technol.* **50**, 5589–5596 (2016).
40. J. W. Chen, K. G. Chan, Genome sequence of *Dyella japonica* strain A8, a quorum-quenching bacterium that degrades N-acylhomoserine lactones, isolated from Malaysian tropical soil. *J. Bacteriol.* **194**, 6331 (2012).
41. H. L. Buss, A. Lüttge, S. L. Brantley, Etch pit formation on iron silicate surfaces during siderophore-promoted dissolution. *Chem. Geol.* **240**, 326–342 (2007).
42. U. Schwertmann, R. M. Taylor, "Iron oxides" in *Minerals in Soil Environments*, J. B. Dixon, S. B. Weed, Eds. (Soil Science Society of America Book Series, Soil Science Society of America, Madison, WI, 1989), vol. 1, pp. 379–437.
43. L. Sigg, W. Stumm, The interaction of anions and weak acids with the hydrous goethite (α -FeOOH) surface. *Colloids Surf.* **2**, 101–117 (1981).
44. L. Wu, A. D. Jacobson, M. Hausner, Characterization of elemental release during microbe-granite interactions at $T = 28^\circ\text{C}$. *Geochim. Cosmochim. Acta* **72**, 1076–1095 (2008).
45. B. Frey et al., Weathering-associated bacteria from the Damma glacier forefield: Physiological capabilities and impact on granite dissolution. *Appl. Environ. Microbiol.* **76**, 4788–4796 (2010).
46. W. W. Barker, S. A. Welch, S. Chu, J. F. Banfield, Experimental observations of the effects of bacteria on aluminosilicate weathering. *Am. Mineral.* **83**, 1551–1563 (1998).
47. L. J. Liermann et al., Microenvironments of pH in biofilms grown on dissolving silicate surfaces. *Chem. Geol.* **171**, 1–16 (2000).
48. P. Vandevivere, S. A. Welch, W. J. Ullman, D. L. Kirchman, Enhanced dissolution of silicate minerals by bacteria at near-neutral pH. *Microb. Ecol.* **27**, 241–251 (1994).
49. B. E. Kalinowski et al., X-ray photoelectron evidence for bacteria-enhanced dissolution of hornblende. *Geochim. Cosmochim. Acta* **64**, 1331–1343 (2000).
50. L. J. Liermann, B. E. Kalinowski, S. L. Brantley, J. G. Ferry, Role of bacterial siderophores in dissolution of hornblende. *Geochim. Cosmochim. Acta* **64**, 587–602 (2000).
51. J. B. Neillands, Siderophores: Structure and function of microbial iron transport compounds. *J. Biol. Chem.* **270**, 26723–26726 (1995).
52. H. L. Buss, R. Mathur, A. F. White, S. L. Brantley, Phosphorus and iron cycling in deep saprolite, Luquillo Mountains, Puerto Rico. *Chem. Geol.* **269**, 52–61 (2010).
53. A. K. Navarre-Sitchler et al., Porosity and surface area evolution during weathering of two igneous rocks. *Geochim. Cosmochim. Acta* **109**, 400–413 (2013).
54. R. A. Berner, E. L. Sjöberg, M. A. Velbel, M. D. Krom, Dissolution of pyroxenes and amphiboles during weathering. *Science* **207**, 1205–1206 (1980).
55. I. Barshad, F. M. Kishk, Oxidation of ferrous iron in vermiculite and biotite alters fixation and replaceability of potassium. *Science* **162**, 1401–1402 (1968).
56. R. J. Gilkes, R. C. Young, J. P. Quirk, Artificial weathering of oxidized biotite: I. Potassium removal by sodium chloride and sodium tetraphenylboron solutions. *Soil Sci. Soc. Am. J.* **37**, 25–28 (1973).
57. R. J. Gilkes, R. C. Young, J. P. Quirk, Artificial weathering of oxidized biotite: II. Rates of dissolution in 0.1, 0.01, 0.001M HCl. *Soil Sci. Soc. Am. J.* **37**, 29–33 (1973).
58. G. Y. Jeong, H. B. Kim, Mineralogy, chemistry, and formation of oxidized biotite in the weathering profile of granitic rocks. *Am. Mineral.* **88**, 352–364 (2003).
59. S. F. Murphy et al., Chemical weathering in a tropical watershed, Luquillo Mountains, Puerto Rico: II. Rate and mechanism of biotite weathering. *Geochim. Cosmochim. Acta* **62**, 227–243 (1998).
60. L. L. Stookey, Ferrozine—A new spectrophotometric reagent for iron. *Anal. Chem.* **42**, 778–781 (1970).
61. C. Bolland, A. Poszwa, C. Leyval, C. Mustin, Dissolution rates of phyllosilicates as a function of bacterial metabolic diversity. *Geochim. Cosmochim. Acta* **74**, 5478–5493 (2010).
62. J. Zhou, M. A. Bruns, J. M. Tiedje, DNA recovery from soils of diverse composition. *Appl. Environ. Microbiol.* **62**, 316–322 (1996).
63. D. E. Wood, S. L. Salzberg, Kraken: Ultrafast metagenomic sequence classification using exact alignments. *Genome Biol.* **15**, R46 (2014).
64. Y. Peng, H. C. Leung, S. M. Yiu, F. Y. Chin, IDBA-UD: A de novo assembler for single-cell and metagenomic sequencing data with highly uneven depth. *Bioinformatics* **28**, 1420–1428 (2012).
65. D. D. Kang, J. Froula, R. Egan, Z. Wang, MetaBAT, an efficient tool for accurately reconstructing single genomes from complex microbial communities. *PeerJ* **3**, e1165 (2015).
66. D. H. Parks, M. Imelfort, C. T. Skennerton, P. Hugenholtz, G. W. Tyson, CheckM: Assessing the quality of microbial genomes recovered from isolates, single cells, and metagenomes. *Genome Res.* **25**, 1043–1055 (2015).
67. S. F. Altschul, W. Gish, W. Miller, E. W. Myers, D. J. Lipman, Basic local alignment search tool. *J. Mol. Biol.* **215**, 403–410 (1990).
68. G. V. Uritskiy, J. DiRuggiero, J. Taylor, MetaWRAP—A flexible pipeline for genome-resolved metagenomic data analysis. *Microbiome* **6**, 158 (2018).
69. S. Kumar, M. Jones, G. Koutsovoulos, M. Clarke, M. Blaxter, Blobology: Exploring raw genome data for contaminants, symbionts and parasites using taxon-annotated GC-coverage plots. *Front. Genet.* **4**, 237 (2013).